



HAL
open science

Auroral kilometric radiation diurnal, semidiurnal, and shorter-term modulations disentangled by Cassini

Laurent Lamy, Philippe Zarka, Baptiste Cecconi, Renée Prangé

► **To cite this version:**

Laurent Lamy, Philippe Zarka, Baptiste Cecconi, Renée Prangé. Auroral kilometric radiation diurnal, semidiurnal, and shorter-term modulations disentangled by Cassini. *Journal of Geophysical Research Space Physics*, 2010, 115 (A09221), pp.9221. 10.1029/2010JA015434 . hal-03732637

HAL Id: hal-03732637

<https://hal.science/hal-03732637>

Submitted on 8 Sep 2022

HAL is a multi-disciplinary open access archive for the deposit and dissemination of scientific research documents, whether they are published or not. The documents may come from teaching and research institutions in France or abroad, or from public or private research centers.

L'archive ouverte pluridisciplinaire **HAL**, est destinée au dépôt et à la diffusion de documents scientifiques de niveau recherche, publiés ou non, émanant des établissements d'enseignement et de recherche français ou étrangers, des laboratoires publics ou privés.

Copyright

Auroral kilometric radiation diurnal, semidiurnal, and shorter-term modulations disentangled by Cassini

L. Lamy,^{1,2} P. Zarka,² B. Cecconi,² and R. Prangé²

Received 5 March 2010; revised 10 May 2010; accepted 24 May 2010; published 28 September 2010.

[1] During the flyby of the Earth by Cassini in 1999, the Radio and Plasma Wave Science (RPWS) instrument recorded a month of quasi-continuous observations of auroral kilometric radiation (AKR). Analyzing the full polarization of incoming radio waves, we found AKR to be 100% circular left-handed (LH) or right-handed (RH). As AKR is emitted predominantly on the extraordinary mode, we analyzed separately the northern (RH) emission, from the southern (LH) one with respect to the magnetic equator. AKR power variations reveal (1) a log-normal distribution at time scales of minutes, (2) bursts of emission at time scales of a few hours, and (3) a clear overall modulation at 24 h, together with a weaker modulation at 12 h (especially visible for LH emissions). The prominent 24 h modulation is found to modulate LH and RH AKR in phase opposition. This is interpreted as being due to visibility effects related to the precession of the terrestrial magnetic dipole, making Cassini oscillate relative to the average AKR beaming pattern from each hemisphere. We accordingly quantified the AKR beaming as a function of explored latitudes. On time scales shorter than a few hours, LH and RH emissions are found to be correlated. This is attributed to the actual conjugacy of the corresponding sources, simultaneously turned on by substorm occurrence. The geometrical anticorrelation (at 24 h) dominates close to Earth, while the short-term correlation (substorms) dominates far from Earth, where the detection threshold makes the visibility less important than the occurrence of substorms. Finally, the 12 h modulation is detected when it is not masked by strong visibility effects, namely, for the LH emission, which is observed mostly near the magnetic equator along the path of Cassini. As a 12 h modulation of some geomagnetic indices was also observed, we suggest that the AKR semidiurnal modulation may have a physical cause, for which we favor the variable geometry and efficiency of the reconnection between interplanetary and geomagnetic fields, or magnetotail oscillations.

Citation: Lamy, L., P. Zarka, B. Cecconi, and R. Prangé (2010), Auroral kilometric radiation diurnal, semidiurnal, and shorter-term modulations disentangled by Cassini, *J. Geophys. Res.*, 115, A09221, doi:10.1029/2010JA015434.

1. Introduction

[2] Auroral kilometric radiation (AKR) is the most intense radio emission from the Earth's magnetosphere. This cyclotron emission covers a spectrum extending over the range ~50–700 kHz, peaking around 200 kHz [Benediktov *et al.*, 1965; Gurnett, 1974], and its typical radiated power lies between 10^7 and 10^9 W [Zarka, 1998]. AKR is mostly produced on the extraordinary (X) magneto-ionic mode, and marginally on the ordinary mode (O), typically 2 orders of magnitude lower, from sources in both hemispheres [Mellott *et al.*, 1984]. This emission has dominant circular polariza-

tion, right-handed (RH) from the northern magnetic (i.e., southern geographic) hemisphere, and left-handed (LH) from the other one [Kaiser *et al.*, 1978]. Radio sources are located at altitudes of 0.5 to ~3 R_E (Earth radii, 1 R_E = 6378 km), above hot spots in the auroral oval [Huff *et al.*, 1988], along high-latitude (~70°) nightside magnetic field lines and around 2300 Local Time (LT) [Gallagher and Gurnett, 1979].

[3] AKR generation is attributed to the Cyclotron Maser Instability (CMI), which amplifies radio waves at the local electron gyrofrequency f_{ce} at large angles from the magnetic field in the source, i.e., along widely open hollow conical beams [Wu and Lee, 1979; Wu, 1985; Treumann, 2000].

[4] Refraction effects along the ray path, at the boundaries of auroral cavities and through the plasmasphere, may generate a complex oblique cone of emission (nonaxisymmetric, partially filled), expected to vary with time (auroral activity, electron density) and source location (frequency, magnetic latitude) [Louarn and Le Quéau, 1996a, 1996b; Xiao *et al.*, 2007; Mutel *et al.*, 2008]. The resulting average beaming pattern of northern and southern AKR sources thus appears as

¹Space and Atmospheric Physics, Imperial College London, London, UK.

²LESIA, Observatoire de Paris, CNRS, UPMC, Université Paris Diderot, Meudon, France.

a broad conical beam, centered on the magnetic vector of the source region, and illuminating approximately one hemisphere. These average beams are tilted toward the nightside, where they leave empty a near-equatorial shadow zone out to $\sim 12 R_E$ [Gallagher and Gurnett, 1979; Green and Gallagher, 1985; LaBelle et al., 1989]. Beyond $\sim 12 R_E$ on the nightside, a near-equatorial observer (at magnetic latitudes lower than 12°) sees superimposed LH and RH emissions, while an observer at higher latitude detects pure RH or LH emission [see Gallagher and Gurnett, 1979, Figure 8].

[5] AKR is an indicator of discrete auroral precipitations, therefore subject to temporal variations on various scales. At short time scales (less than a few hours), it intensifies during substorms [Kurth et al., 2001], leading to nightside magnetic reconnection events in the Earth's magnetotail, driven by varying solar wind and interplanetary magnetic field (IMF) conditions [Alexander and Kaiser, 1977; Gallagher and Dangelo, 1981]. The auroral activity and AKR sources are thus mainly confined to nightside LT, where they are not affected by corotation effects, in contrast with, for instance, the Jovian radio sources [Zarka, 1998]. At longer time scales, diurnal and seasonal modulations of the auroral activity have been observed [Berthelier, 1976], as well as seasonal variations of the AKR intensity and spectrum [Kasaba et al., 1997; Kumamoto et al., 2003; Green et al., 2004]. However, to our knowledge, no AKR diurnal variation had been reported until the Earth flyby of the Cassini spacecraft in August 1999. At this occasion, the Radio and Plasma Wave Science (RPWS) experiment revealed an unexpected strong periodic modulation of the AKR signal at 24 h [Lamy et al., 2007], which was confirmed by observations from the STEREO-B spacecraft in 2007 [Panchenko et al., 2009].

[6] This finding raises questions on the origin of the modulation, which can be related either to (A) actual variations of radio sources, or to (B) visibility effects. The former includes any clock-like rotational modulation of the triggering process of fixed LT sources (as on Saturn). The latter may include (B₁) a rotation of the emission beam, similar to that of a searchlight (as on Jupiter, but inconsistent with AKR sources being fixed on the nightside); (B₂) a geometrical oscillation, in the spacecraft reference frame, of the beam radiated by sources fixed in LT, related to the tilt between the magnetic and rotational axes; or (B₃) a periodic variation of the final direction of the beam due to its refraction in a similarly precessing plasmasphere.

[7] In this article, we present a detailed analysis of AKR properties, as derived from the RPWS instrument onboard Cassini, focussing on time variations. Section 2 details the observation geometry, the instrumentation, and the radio data processing. Section 3 focuses on the AKR polarization state, spectrum and intensity distribution. In section 4, we extensively analyze AKR temporal modulations for time scales ranging from less than 1 h to 24 h, for which interpretations are discussed in section 5.

2. Cassini Trajectory, Instrumentation, and Data Processing

2.1. Cassini Ephemeris

[8] The Cassini spacecraft performed a close flyby of the Earth on 18 August (day 230) 1999, during which RPWS recorded 31 days of quasi-continuous AKR observations,

from day 227 to day 257 (15 August to 14 September), while Cassini traveled at $\sim 9 R_E/h$, from $1.2 R_E$ to $\sim 6400 R_E$. This corresponded to late summer conditions for the northern rotational (southern magnetic) hemisphere. The inbound trajectory was in the 1230 LT meridian at 2° ecliptic latitude, and the outbound one lied between 0100 and 0200 LT at -2° ecliptic latitude (see Figure 1). The relevant coordinate system that we will use hereafter is the magnetic coordinate system. The terrestrial magnetic dipole is nearly opposite to the planetary rotation axis, with the south magnetic pole at the center of the aurora borealis region at a longitude of 71.78° west and a northern latitude of 79.74° (in geographic coordinates). We will count positively the magnetic latitudes (noted λ_{mag}) in the northern magnetic hemisphere, i.e., the southern rotational hemisphere. With this convention, the outbound leg of Cassini's trajectory oscillated between $\lambda_{sc,mag} = -15^\circ$ and $+5^\circ$ (Figures 1d and 2).

2.2. Radio Instrument

[9] The RPWS experiment includes a High Frequency Receiver (HFR), measuring AC electric fields between 3.5 kHz and 16.125 MHz, which can be connected to 2 inputs chosen among 3 monopole antennas and one dipole synthesized by two monopoles [Gurnett et al., 2004]. The receiver computes autocorrelation and cross correlation of its input signals, from which goniopolarimetric (GP) inversions [Cecconi and Zarka, 2005] enable to retrieve the wave intensity and polarization state (Stokes parameters S, Q, U, V) as well as its direction of arrival (\mathbf{k} vector defined by two angles θ and ϕ). Two-antenna measurements allow us to perform full polarization measurements (S, Q, U, V) or goniometric measurements plus circular polarization (S, V, θ , ϕ). When, in addition, the receiver switches rapidly between the 3 monopole inputs, full GP measurements (S, Q, U, V, θ , ϕ) can be performed. In all cases, each instantaneous measurement at a given frequency characterizes the polarization and direction of arrival of waves radiated by the most intense point source detected at that time and frequency.

2.3. Data Processing

[10] In this article, we analyze the Stokes parameters (S, Q, U, V) derived from two-antenna measurements in polarimeter mode (with the source direction set at Earth's center) [Cecconi and Zarka, 2005].

[11] Figure 3 displays a typical example of dynamic spectra of the radio flux density S and corresponding circular polarization V measured by RPWS/HFR on day 232, between 3.5 kHz and 1.5 MHz. Flux density measurements reveal strong AKR bursts between ~ 100 and ~ 500 kHz, superposed on Solar type III bursts and low-frequency (often electrostatic) bursts and noise. Weak bursts of emission about 1 MHz are also visible near 0400 UT and 1000 UT. In Figure 3b, AKR is the only emission to show up with strong RH or LH circular polarization (red and blue, respectively), together with the weak bursts at ~ 1 MHz, identified as the hectometer (HOM) emission of Jupiter [Zarka et al., 2004]. The other emissions, including the Solar type III bursts, which are unpolarized, cannot be distinguished from the background.

[12] As a first step, we investigated quantitatively the AKR polarization state in section 3.1 (Figure 4). This analysis was performed over all available two-antenna measurements,

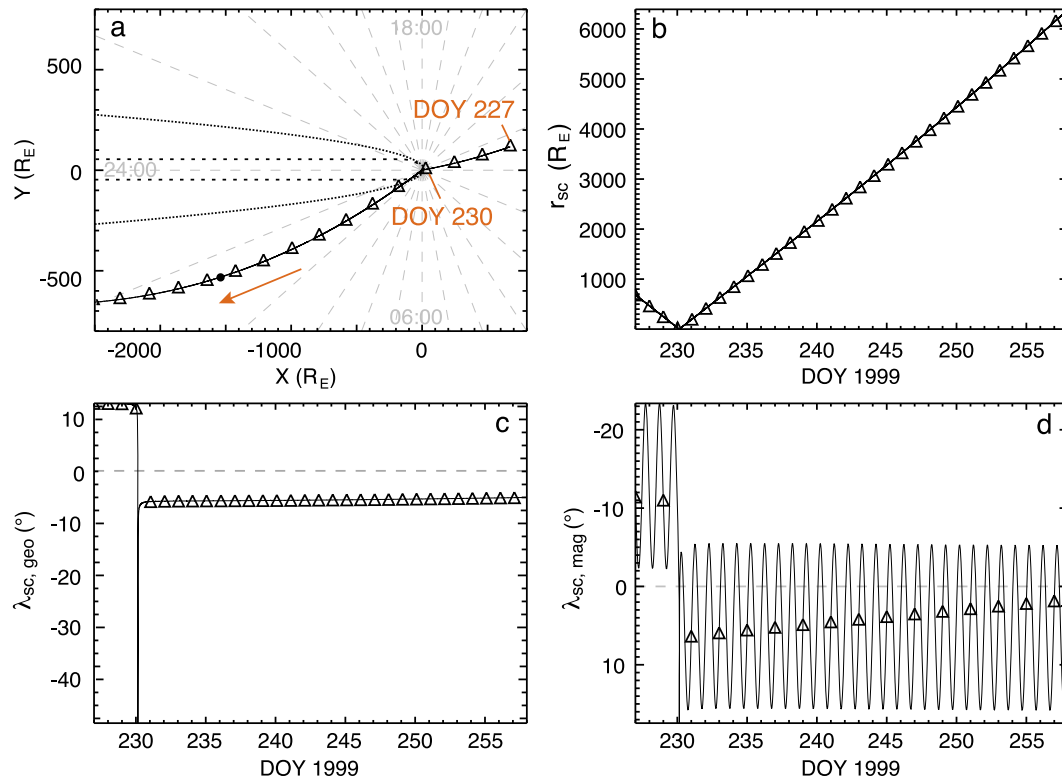


Figure 1. Trajectory of Cassini in August 1999 during the Earth flyby. (a) Projection on the ecliptic plane. The Sun is to the right. The Earth's magnetosphere and bow shock are sketched with dashed and dotted lines, respectively. Triangles mark round days of year (DOY) 1999 (at 0000 UT) along the trajectory of Cassini. Gray numbers indicate LT. The black dot marks the transition between anticorrelated and correlated RH and LH AKR (see text). (b) Cassini-Earth distance versus time. (c) Geographic latitude of Cassini versus time. (d) Magnetic latitude of Cassini versus time.

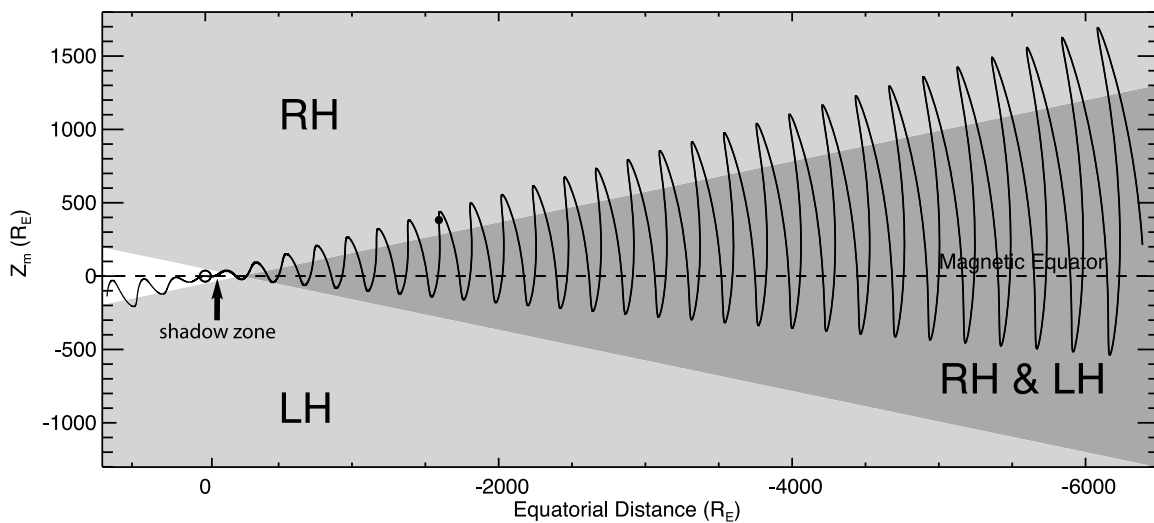


Figure 2. Sketch of the path of Cassini in magnetic coordinates in two half-meridian planes (separately for the inbound and outbound legs), superimposed onto the regions illuminated by northern (RH) and southern (LH) AKR. Sun is to the left. The Earth (not to scale) lies at (0,0). The equatorial AKR shadow zone (enlarged here by a factor $\times 20$ and frequency dependent) is filled in white, regions illuminated by either RH or LH sources in light gray, and the region illuminated by both sources in darker gray. The limit magnetic latitude of these regions, placed here at $\sim 12^\circ$, is only indicative and subject to a $\pm 3^\circ$ uncertainty. The black dot marks the transition between anticorrelated and correlated RH and LH AKR (see text), as in Figure 1.

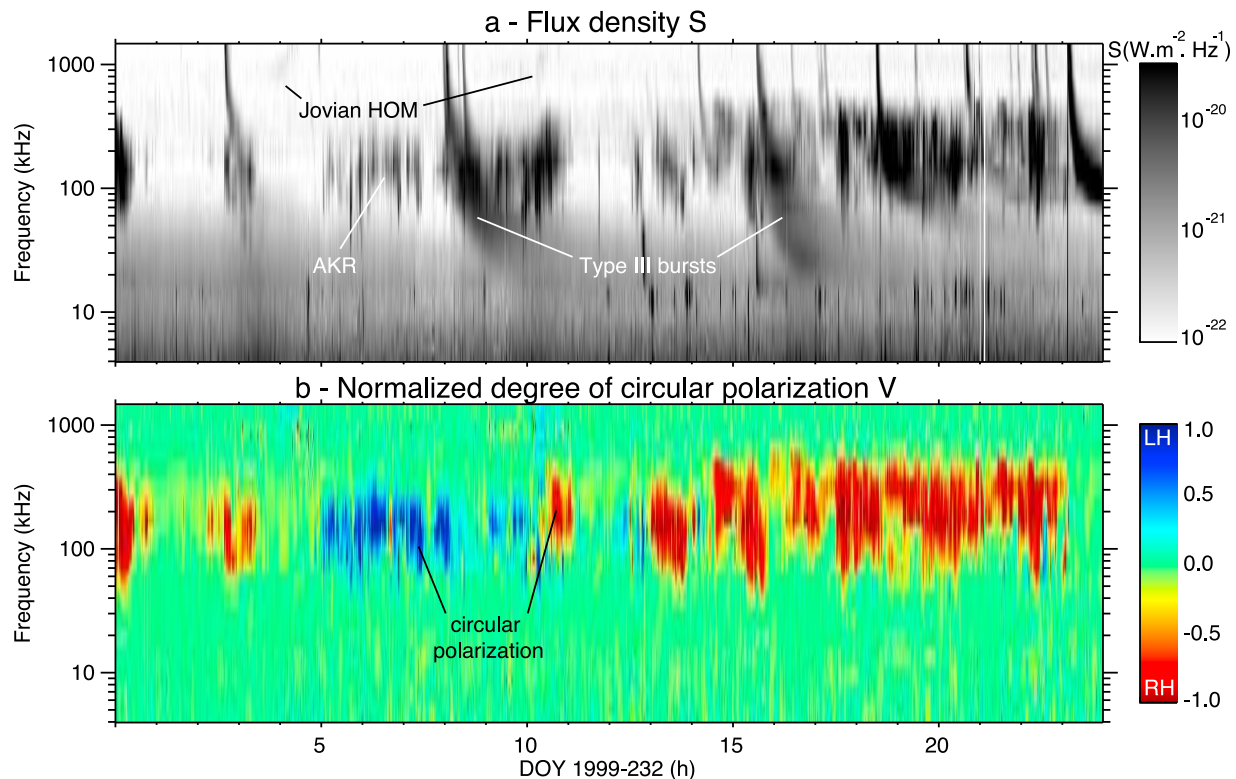


Figure 3. (a) Flux density and (b) circular polarization measured between 3.5 kHz and 1.5 MHz on day 232, displayed as a function of time and frequency. The displayed parameters have been computed with RPWS/HFR two-antenna measurements in polarimeter mode and the source direction set at the Earth’s center, after manual removal of RFI (for clarity). In Figure 3b, the range 500–1500 kHz has been recomputed separately with the source direction set at Jupiter, revealing mainly RH and then LH circularly polarized emission, coming from Jupiter’s northern and southern hemispheres.

with a careful selection on parameters known to affect goniopolarimetric results, such as the signal-to-noise ratio (SNR) on each of the two antennas, and the angle β , between the antenna plane and the direction of the wave (approximated by the Earth-Cassini direction in polarimeter mode) [Cecconi and Zarka, 2005]. We chose standard criteria: $\text{SNR} \geq 15$ dB, largely satisfied within AKR bursts (often observed with SNR above 20 dB), and $|\beta| \geq 20^\circ$, corresponding to $\sim 90\%$ of measurements (while $\sim 9\%$ were recorded with $15^\circ \leq |\beta| \leq 20^\circ$, and $\sim 1\%$ with $|\beta| \leq 15^\circ$) [Cecconi, 2009].

[13] As a second step, we focussed on the AKR intensity and modulations in sections 3.2 and 4 (Figures 5–14). For those studies, we needed as many data as possible for statistical conclusions to be drawn, and we needed to identify unambiguously RH and LH AKR emissions, in order to analyze them separately. Instead of the above severe data selection, which would reduce the size of the database too much, we used the property of AKR to be strongly circularly polarized (see Figure 3b) in order to automatically extract AKR emissions thanks to the single criterion $|V| \geq 0.2$. As radio frequency interference (RFI) and solar type III bursts are unpolarized, this simple data selection is enough to eliminate most RFI and all solar emissions down to an intensity ~ 6 dB above that of simultaneous AKR. Lower level spurious emissions are not removed, but their superposition to AKR cannot change the measured sign of V . They could, at most,

result in a slight overestimate of the AKR level, which has very little impact on the long-term time series and on their statistical analysis. Note that, on Figure 3, the AKR bursts exhibit a high SNR (≥ 20 dB), that the distribution of V inside each burst is quite homogeneous (highly positive or negative), and that the blobs are surrounded by a thin region of decreasing V magnitude but of the same sign. The sign of the

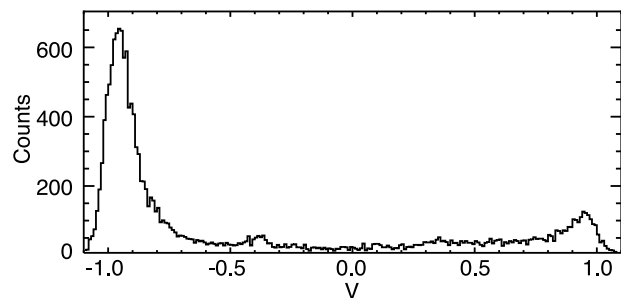


Figure 4. Distribution of the circular polarization degree V measured from polarimetric two-antenna measurements spread over the whole month of Cassini observations at Earth, over a selection of time intervals containing only AKR (i.e., excluding solar emissions), between 40 and 500 kHz, and satisfying the criteria $\text{SNR} \geq 15$ dB for each antenna, and $\beta \geq 20^\circ$.

circular polarization thus appears unambiguous inside the AKR bursts and can be reliably used as a selection criterion in the studies of AKR intensity. This approach was described and used by *Lamy et al.* [2008a] to extract Saturn's radio emissions. Then, we built continuous, calibrated dynamic spectra of the received flux densities (S in $\text{W m}^{-2} \text{Hz}^{-1}$, normalized to 1 AU) and circular polarization degree (V), as well as apparent radiated powers (P in W sr^{-1}), computed after applying a $1/r_{sc}^2$ correction (r_{sc} being the Cassini-Earth distance), and integrating over each individual HFR frequency channel (~ 1 to 50 kHz wide). These dynamic spectra have homogeneous resolutions in time (90 s) and frequency (24 log-spaced channels between 3.5 and 320 kHz with $\delta f/f = 20\%$, and 24 linearly spaced channels between 350 and 1500 kHz with $\delta f = 50$ kHz).

3. AKR Stokes Parameters

3.1. Polarization State

[14] In this section, we analyze the AKR full polarization state. To avoid contamination by intense unpolarized emissions, sometimes superimposed to the AKR pattern (see Figure 4), we first selected manually time intervals containing AKR only, over the [40,500 kHz] spectral range, i.e., we eliminated systematically all the intervals where Solar type III bursts or strong interference were present, on top or in the vicinity of AKR blobs. Then, we used the standard data selection criteria described in section 2.3 ($\text{SNR} \geq 15$ dB and $|\beta| \geq 20^\circ$), to obtain reliable measurements of all Stokes parameters.

[15] Figure 4 displays the resulting distribution of circular polarization degree V , that exhibits a main peak at $V = -0.96 \pm 0.06$ (RH circular polarization), and a secondary one about $V = +0.94 \pm 0.06$ (LH circular polarization), above a low-average background distribution in between ($\sim 5\%$ and $\sim 30\%$ of the RH and LH peaks, respectively). Within this background, a few % of the measurements exhibit linear polarization, that we checked to be of instrumental origin (linear polarization degree $\neq 0$ is only observed on one pair of RPWS antennas, and varies systematically with β , that does not overcome 25°). These results show that AKR observed from low latitudes is almost purely circularly polarized, and confirm previous studies at higher latitudes [*Panchenko et al.*, 2008, and references therein]. In addition, this legitimates the use of a $|V| \geq 0.2$ threshold to automatically extract AKR emission.

[16] Note that AKR polarization differs from that of kronian SKR, the latter being measured purely circular from low latitudes ($\geq 30^\circ$) [*Lamy et al.*, 2008a], but elliptical from higher latitudes [*Fischer et al.*, 2009].

3.2. Intensity and Spectrum

[17] For intensity and spectra studies that follow, we used the database described in section 2.3 (data selection with $|V| \geq 0.2$ only).

[18] Figure 5 displays dynamic spectra of RH and LH flux densities, normalized to an observer's distance of 1 AU, and circular polarization degree of AKR, over the entire flyby. Under the assumption that AKR X mode is predominant, RH and LH emissions originate from the northern and southern magnetic hemisphere, respectively. The most intense emis-

sions are observed after closest approach (CA, on day 230) along the outbound leg, consistent with the assumption of nightside AKR sources. RH polarization dominates as expected, since Cassini spent most of its time in the northern magnetic hemisphere (Figures 1d and 2). AKR normalized intensity (and, following, spectral bandwidth) decreases with decreasing SNR, corresponding to increasing distance to Earth.

[19] Figure 6a displays the flux densities reached by RH and LH AKR 50, 10 and 1% of the time, corresponding to increasing intensity thresholds, as a function of frequency. The spectrum extends from ~ 30 to 650 kHz. Signals below 30 kHz are due to local emissions mostly detected near CA (days 230 to 235 in Figure 5). All spectra exhibit a typical shape with a slow increase followed by a sharp drop. It is interesting again to note that the AKR spectra are remarkably similar in shape to the SKR ones observed at low latitudes ($|\lambda_{sc, \text{mag}}| \leq 30^\circ$) at Saturn by Cassini (see, for comparison, Figures 8a and 8c of *Lamy et al.* [2008a]). The intensity increases by nearly 2 orders of magnitude between the 50% (average) and 1% (peak) levels, while the spectrum extent slightly broadens, with a frequency of the peak increasing from ~ 200 to ~ 300 kHz.

[20] The evolution of the spectrum extent with intensity is quantified in Figure 6b, that shows the ratios of the spectra of Figure 6a between 30 and 650 kHz. For both RH and LH components, the 10% to 50% and 1% to 10% ratios remain approximately flat between 100 and 200 kHz, while they show a clear positive slope toward higher frequencies, and, to a lesser degree, toward lower frequencies. This suggests that the most intense AKR sources are observed over a broader altitude range, especially toward lower altitudes (larger f_{ce}). This can result either from a visibility effect related to a variable beaming angle (relative to the magnetic field) or from an increase of the CMI efficiency (e.g., deeper penetration of auroral cavities into the denser ionospheric plasma).

[21] As both the beaming pattern and the location of the observer with respect to the emission cone are unknown, it is not possible to retrieve the real power radiated by the source from the measured flux densities. We could therefore only derive the average power radiated by the AKR source in the direction of the observer (in W sr^{-1}) measured in individual HFR channels P_{RH} and P_{LH} . The directional radiated power (or apparent power) distributions are found to be close to log-normal ones, with an average of $P_{RH} = 2 \times 10^6 \text{ W sr}^{-1}$ and $P_{LH} = 8 \times 10^5 \text{ W sr}^{-1}$, a standard deviation of ~ 10 , and no obvious dependence in frequency over the AKR spectrum. After integration over the appropriate band 30–650 kHz, we obtained the distributions of spectrum-integrated AKR powers shown in Figure 7. A best fit log-normal curve was superimposed (dashed line). The agreement with the observed distribution is generally good. The LH emission power derived from the measurements is only slightly distorted toward low power values at both ends of the distribution. The fit is almost perfect for the RH emission power distribution, for a large upper range of the distribution (both sides of the peak), probably due to a better statistics. The observed low power distribution is also above the log-normal best fit curve, but not significantly since the scale is logarithmic.

[22] The average of the directional radiated power distributions are $P_{RH} = 1.5 \times 10^7 \text{ W sr}^{-1}$ (maximum RH power

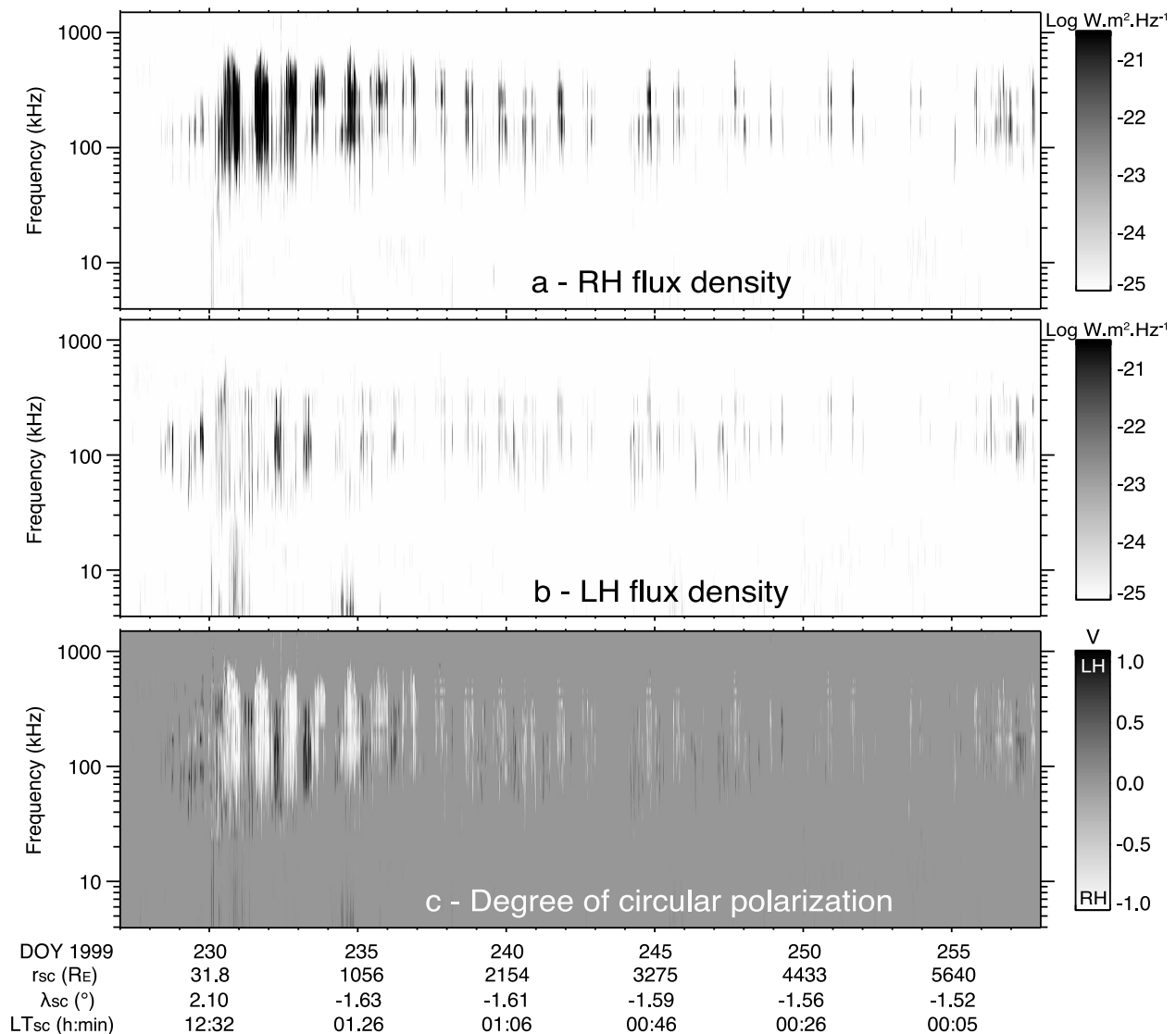


Figure 5. Dynamic spectra of (a) RH and (b) LH AKR flux densities S normalized to 1 AU over the entire flyby. (c) Circular polarization degree V , from purely RH (white) to purely LH (black). S_{RH} , S_{LH} , and V are computed by processing all RPWS/HFR two-antenna measurements in polarimeter mode as described in section 2.3, enabling a continuous coverage while inducing no error due to the dominant circular polarization of AKR. The ephemeris of Cassini are indicated in abscissa: r_{sc} , λ_{sc} , and LT_{sc} indicate the distance to Earth, the ecliptic latitude, and the LT of the spacecraft, respectively.

$\sim 1.3 \times 10^{10} \text{ W sr}^{-1}$) and $P_{LH} = 4 \times 10^6 \text{ W sr}^{-1}$, with again a standard deviation of ~ 10 . The values for P_{LH} are less significant because AKR detected along Cassini's trajectory is largely dominated by RH emission. The values for P_{RH} are fully consistent with (and even in slight excess of) those given by *Benson and Fainberg [1991]* and *Zarka [1998]*.

[23] As displayed in Figures 1d and 2, Cassini mainly explored the range of magnetic latitudes, from -5° to $+15^\circ$ along its postencounter trajectory. As shown in Figure 8 and discussed below, the detected AKR power strongly depends upon the magnetic latitude of the observer. In order to deconvolve this latitudinal dependence from the intrinsic distribution of AKR powers, we recomputed these distributions over restricted, 5° wide, intervals of magnetic latitude. These distributions are again log-normal, with a lower stan-

dard deviation than the latitude-integrated distribution (typically ~ 5). Best fits relevant to each latitude interval are plotted by dotted curves (1) to (4) in Figure 7b. They show that the power distributions are shifted toward lower power values as the magnetic latitude decreases. This analysis was limited to RH AKR because LH emission is swamped in dominant RH emission so that its statistics is unreliable.

[24] Log-normal distributions are characteristic of waves whose final intensity S results from a series of successive amplifications with a large range of growth rates (γ_i) and/or interactions times (δt_i) [*Campbell, 1996*]. In that case, the wave electric field E grows as $\prod_i e^{\gamma_i \delta t_i}$. Thus, the wave intensity, proportional to E^2 , has a logarithmic distribution $\log S$ proportional to $\sum_i \gamma_i \delta t_i$. For a random distribution of γ_i and/or δt_i , $\log S$ will have a normal distribution, according

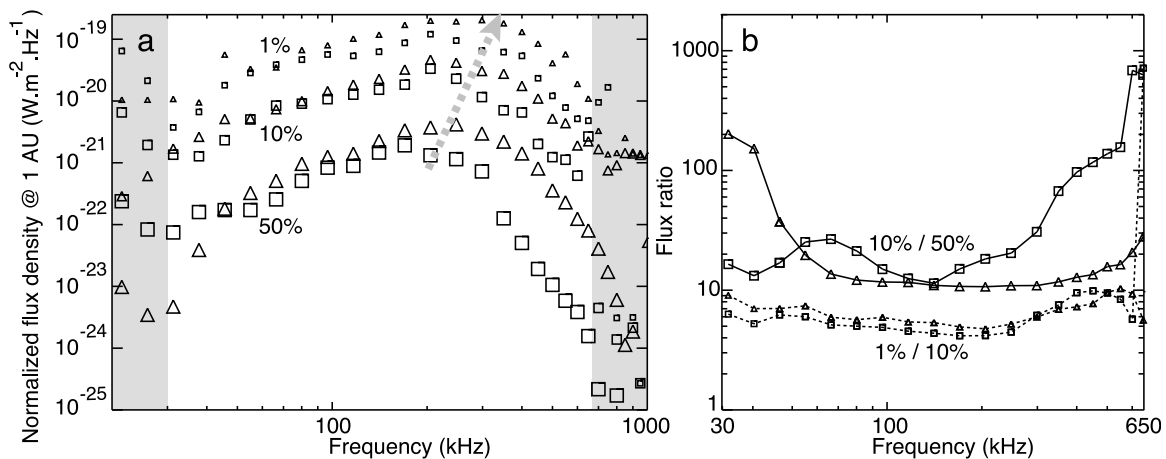


Figure 6. (a) Flux densities normalized to 1 AU reached by AKR 50%, 10%, and 1% of the time, as a function of frequency (big, medium, and small symbols, respectively, corresponding to increasing intensity thresholds). Triangles refer to RH emission, and squares refer to LH emission. RPWS detection threshold was here $\sim 10^{-23} \text{ W m}^{-2} \text{ Hz}^{-1}$. The gray arrow emphasizes the shift of the AKR spectral peak toward higher frequencies with increasing intensity. (b) 10% to 50% ratio and 1% to 10% ratio of the spectra displayed in Figure 6a, between 30 and 650 kHz.

to the central limit theorem. Such distributions have already been observed in the intensity of terrestrial auroral Langmuir waves [Samara *et al.*, 2008] or visible emissions [Shefov *et al.*, 2006]. The above results establish that this also the case for the CMI instability. A more detailed study of the log-normal distribution parameters (out of the scope of this paper) might allow us to estimate an order of magnitude of the growth rate and of the interaction time characteristic of this particular instability. Finally, Figure 8 quantifies the dependence of the RH power with magnetic latitude, i.e., the shape of the equatorial edge of the northern AKR emission diagram. The lin.-log. best fit of this dependence (solid line in Figure 8) can be analytically written as

$$\log P_{RH} (\text{W} \cdot \text{sr}^{-1}) = A + B \times \lambda_{sc, mag} (^{\circ}) \quad (1)$$

with ($A \sim 2$, $B = 0.37$) for long-term integrated RH power (over 3 h), and ($A \sim 4.2$, $B = 0.29$) for short-term integrated RH power (over 15 minutes). An overall representation of the equatorward AKR beam can thus be written as

$$P_{RH} = 10^{2-4} \times 10^{\lambda_{sc, mag} / 3} \quad (2)$$

4. AKR Temporal Modulations

[25] A 24 h periodic modulation of the occurrence of detected AKR is clearly revealed by Figure 5, with finer structure visible inside AKR daily episodes. Quantitatively, Figure 9 displays time series of the RH and LH AKR directional radiated power integrated over the 30–650 kHz range (see section 3.2) and averaged over a 3 h sliding window. The superimposed magnetic latitude of Cassini (gray line), modulated by the Earth’s rotation, can be used as a 24 h clock. The

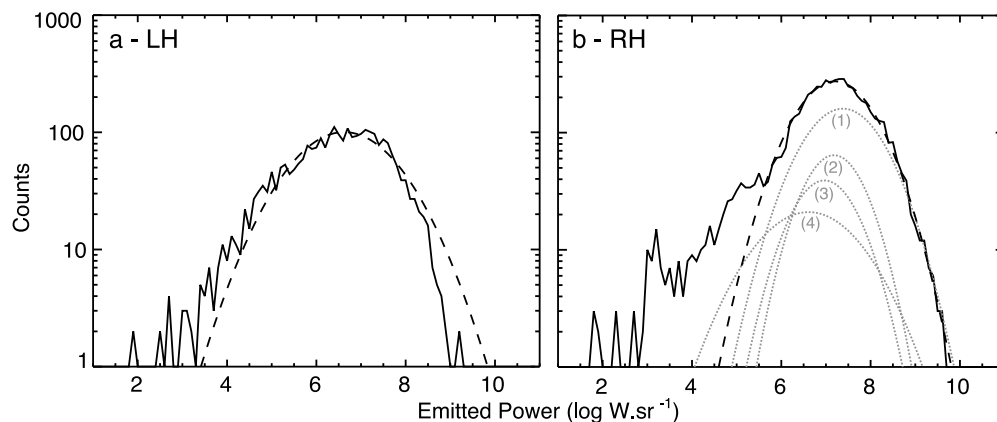


Figure 7. Apparent radiated power distributions of (a) LH and (b) RH AKR emissions, computed as described in section 2 and integrated over 30–650 kHz, fitted by a log-normal function (dashed lines). In Figure 7b, the dotted curves are fits to the RH power distributions computed over the following intervals of Cassini magnetic latitude: (1) [10°, 15°], (2) [5°, 10°], (3) [0°, 5°], (4) [-5°, 0°]. The most dispersed curve (4) corresponds to weak RH emissions close to the background level.

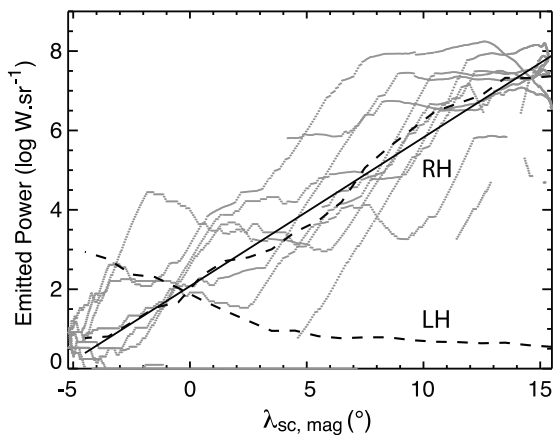


Figure 8. RH AKR apparent radiated power integrated over 30–650 kHz versus Cassini’s magnetic latitude along the outbound path (dotted). The dashed curve is the average per magnetic latitude bin. The solid straight line is the best linear fit to the average dashed curve (in a lin.-log. scale). For LH emission, only the average variation is shown (dashed). It varies symmetrically to the RH one with respect to the magnetic equator, but the latitudinal exploration by Cassini is insufficient for a complete characterization of the southern magnetic AKR beam.

diurnal modulation of AKR power is visible in both polarization states, with peak amplitude variations over several orders of magnitude. In addition, the RH and LH power variations appear anticorrelated until day 237, each polarization state peaking when Cassini is at its maximum latitude in the hemisphere of the corresponding source, i.e., in the best visibility conditions for this source. By contrast, after day 237, RH and LH power variations appear correlated, without any clear relationship with the latitude of Cassini. The approximate transition point is indicated in Figures 1a and 2 by the black dot $\sim 1500 R_E$ away from the Earth.

[26] In order to quantify this trend, we have computed the linear cross-correlation coefficient C of the two profiles P_{RH} and P_{LH} in Figure 10, and of each one with the magnetic latitude variations, using a 5 day sliding window. Powers being in logarithmic scale, the linear correlation is equivalent to a rank correlation. We confirm the above qualitative conclusions about the relative variations of P_{RH} and P_{LH} : we find $C = -0.2$ to -0.3 for a sliding window centered between days 232 and 235, switching to $C \geq 0.6$ between days 238 and 255 (solid line on Figure 10). The dash-dotted line on Figure 10 shows that P_{RH} is correlated to the magnetic latitude of Cassini over the whole encounter, although the correlation coefficient decreases when the distance to Earth increases. Conversely, the dotted line shows that P_{LH} is moderately correlated with the magnetic latitude, albeit with a clear tendency to anticorrelation prior to day 237. This is in agreement with the latitudinal dependence of AKR power found in previous section and Figure 8. We discuss the variability of the correlation between P_{RH} , P_{LH} and the magnetic latitude in the next section. Variations at time scales shorter than 24 h are also visible in Figure 9, for example periodic variations at about 12 h (two peaks per 24 h) in LH power between days 238 and 242, and nonperiodic variations at shorter time scales. We have thus quantified RH and LH

power variations through Fourier analysis. Figure 11 presents power spectra for both polarizations and three time periods. Over the entire flyby (Figures 11a and 11b), a strong narrow peak at 24 h dominates the RH power spectrum. A similar but broader peak shows up in LH power, together with a well-defined narrow peak at 12 h. The average spectral power is much lower in LH than in RH polarization, in agreement with the visibility conditions of AKR sources from both hemispheres along the path of Cassini. Separate analyses of early (Figures 11c and 11d) and late (Figures 11e and 11f) post-encounter intervals confirm the results of Figures 11a and 11b, showing in addition that the occurrence and/or level of short-term fluctuations (≤ 24 h) is variable over the encounter. The well-defined peak at 24 h dominating the RH power spectrum is ubiquitous (Figures 11c and 11e). In LH polarization, a peak at 24 h dominates the early postencounter interval (Figure 11d), while a peak at 12 h dominates the late postencounter interval (Figure 11f). In both cases, peaks at 12 h and 24 h are visible. We also note the presence of smaller spectral power peaks at time scales between ~ 1 and ~ 10 h. In a previous study of AKR power flux variations measured by RPWS, Kurth *et al.* [2001] interpreted them as the signature of substorms, whose recurrence time scale is of the order of a few hours [Borovsky *et al.*, 1993].

[27] The ubiquitous peak at 24 h is necessarily related to the rotation of the Earth, by processes investigated below. The origin of the modulation at 12 h is less obvious: is it a beating of the 24 h modulation, a spurious spectral peak accidentally and temporarily emerging from the superposition of the 24 h modulation and short-term fluctuations, or does it have a true physical origin? An element of response can be obtained from the analysis of external control parameters of AKR activity. We have analyzed the temporal variations of solar wind parameters and of geomagnetic activity indices, by computing their Fourier spectrum over intervals similar to those of Figure 11 as well as their cross correlation with RH and LH AKR variations. For the solar wind, we have studied the fluctuations of the density, velocity, pressure, IMF, and convection electric field across the magnetosphere, averaged over 1 h. We could not find any relationship with the observed variations of AKR, especially at time scales of 12 h and 24 h (except for a transient peak at 24 h in the sliding Fourier spectrum of the electric field). For the geomagnetic indices, we have studied the fluctuations of the indices AL, AU, AE, Dst, Kp and PC, averaged over 1 h.

[28] Ax indices characterize the auroral electrojet via magnetic perturbations measured at several points of the northern auroral zone: AU (AL) is the upper (lower) bound or maximum positive (negative) excursion of the north-south magnetic perturbation over the stations, measuring the eastward (westward) electrojets. Important variations of AE (= AU – AL) characterize magnetospheric substorms. Dst, Kp and PC characterize near-equatorial, midlatitudes, and polar cap magnetic perturbations, respectively (see details at <http://magbase.rssi.ru/REFMAN/SPPHTEXT/indices.html>).

[29] We did not find any significant change of the level of activity indices over the interval 227–258 studied here, but Fourier analysis over the whole interval revealed a peak at 24 h in AU as displayed in Figure 12a (and marginally in PC north). A bias due to the nonuniform distribution of measurement points along the auroral zone cannot be excluded, but Fourier analysis within restricted intervals also reveals

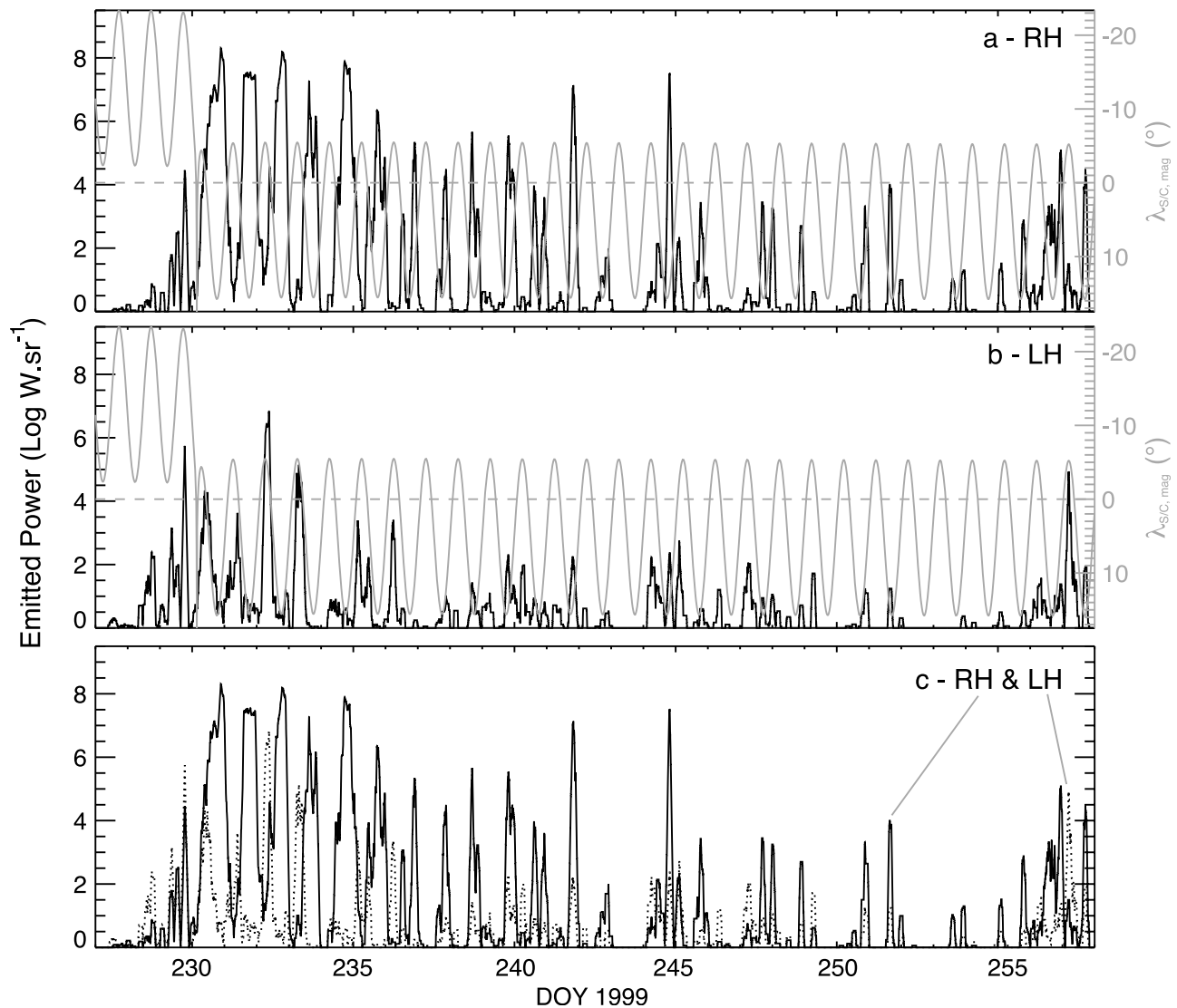


Figure 9. Time series of (a) RH and (b) LH apparent radiated powers integrated over 30–650 kHz, smoothed over 3 h. The magnetic latitude of Cassini is superimposed (gray line, identical in both frames). (c) RH (solid) and LH (dotted) powers are reproduced together.

a nonpermanent peak at 12 h in the AU power spectrum, as displayed in Figure 12b for an interval nearly identical to that of Figure 11f. AU is also the only geomagnetic index for which linear cross correlation with AKR power (over a 5 day sliding window) leads to quasi-permanent correlation at a level $C \sim 0.3$ – 0.6 . Weaker transient correlations were observed for AE, $-AL$, PC, and the solar wind electric field.

[30] We now compare the fluctuations of RH and LH AKR apparent powers over two days of the early (Figure 13, left) and late (Figure 13, right) postencounter path, first at short time scales by smoothing the data over 15 min (Figures 13a and 13b), and then at longer time scales by smoothing them over 3 h (Figures 13c and 13d).

[31] During the early period, the 3 h smoothed RH and LH powers clearly vary in antiphase with diurnal alternance of RH and LH emission (Figure 13c). The maxima of one component correspond to the minima of the other one, so that the LH to RH intensity ratio varies on a diurnal scale with a

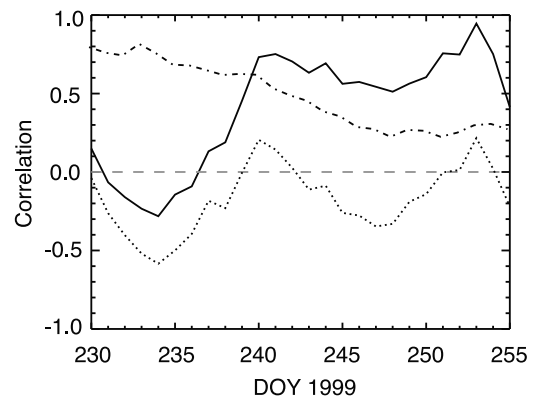


Figure 10. Linear cross correlation, computed with a 5 day sliding window, of the variations of $\log P_{RH}$ and $\log P_{LH}$ (solid line), $\log P_{RH}$ and $\lambda_{sc, mag}$ (dash dotted), and $\log P_{LH}$ and $\lambda_{sc, mag}$ (dotted).

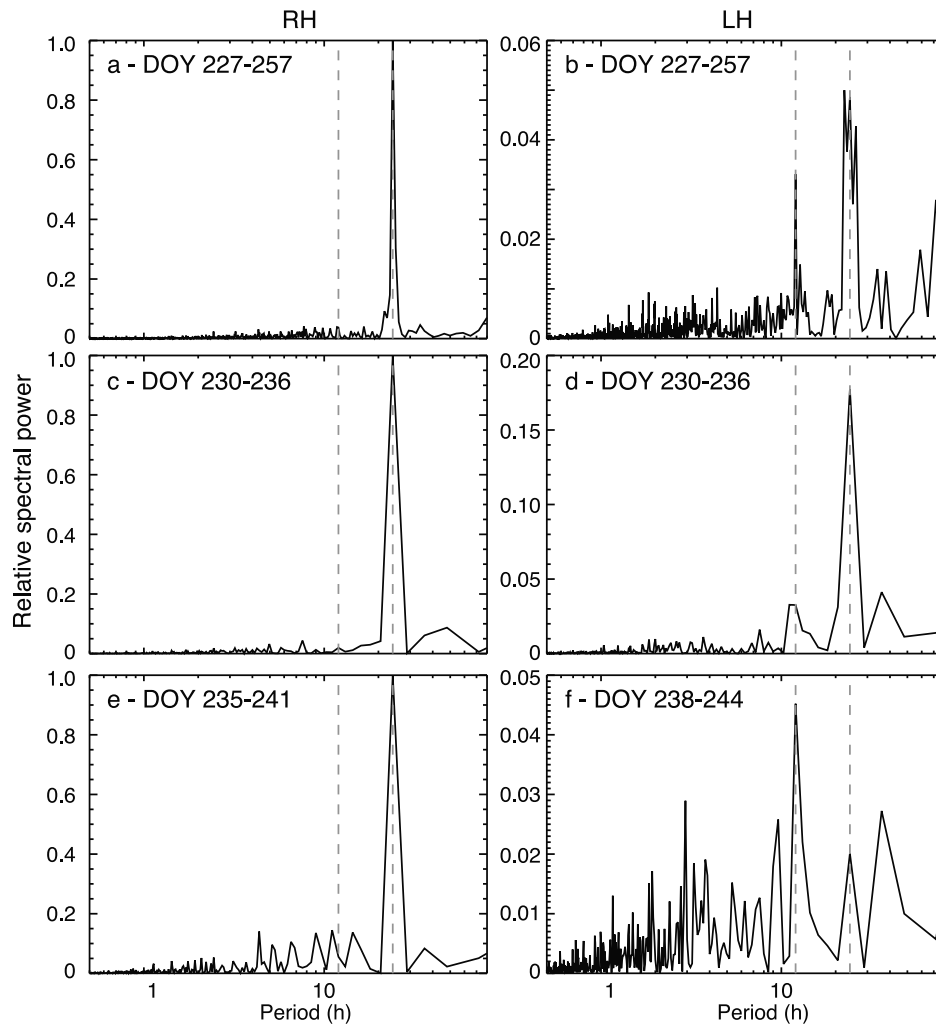


Figure 11. Fourier analysis of RH and LH apparent emission variations (a, b) over the entire flyby and (c–f) during selected postencounter intervals. Power spectra have been computed over time series of $\log P_{RH}$ and $\log P_{LH}$ (integrated over 30–650 kHz, as in Figure 9), in order to give less weight to the variations of the AKR power, which can reach several orders of magnitude. For each row, both RH and LH power spectra have been normalized by the maximum value of the RH power spectrum. Dashed lines indicate 12 and 24 h periods. The horizontal logarithmic scale causes long-period peaks to look artificially broader than short-period ones. Slightly different intervals were selected for Figures 11e and 11f because the resulting spectra were less noisy.

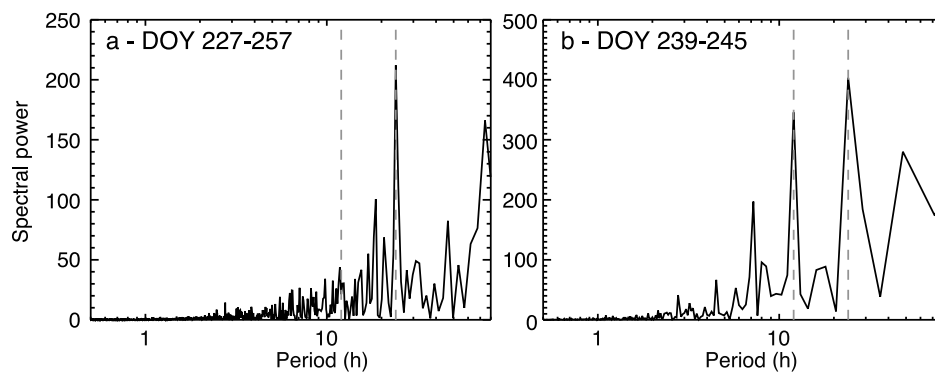


Figure 12. Fourier spectra of the AU geomagnetic index (a) over the entire flyby and (b) during a restricted postencounter interval. Dashed lines indicate 12 and 24 h periods. The horizontal scale is the same as in Figure 11.

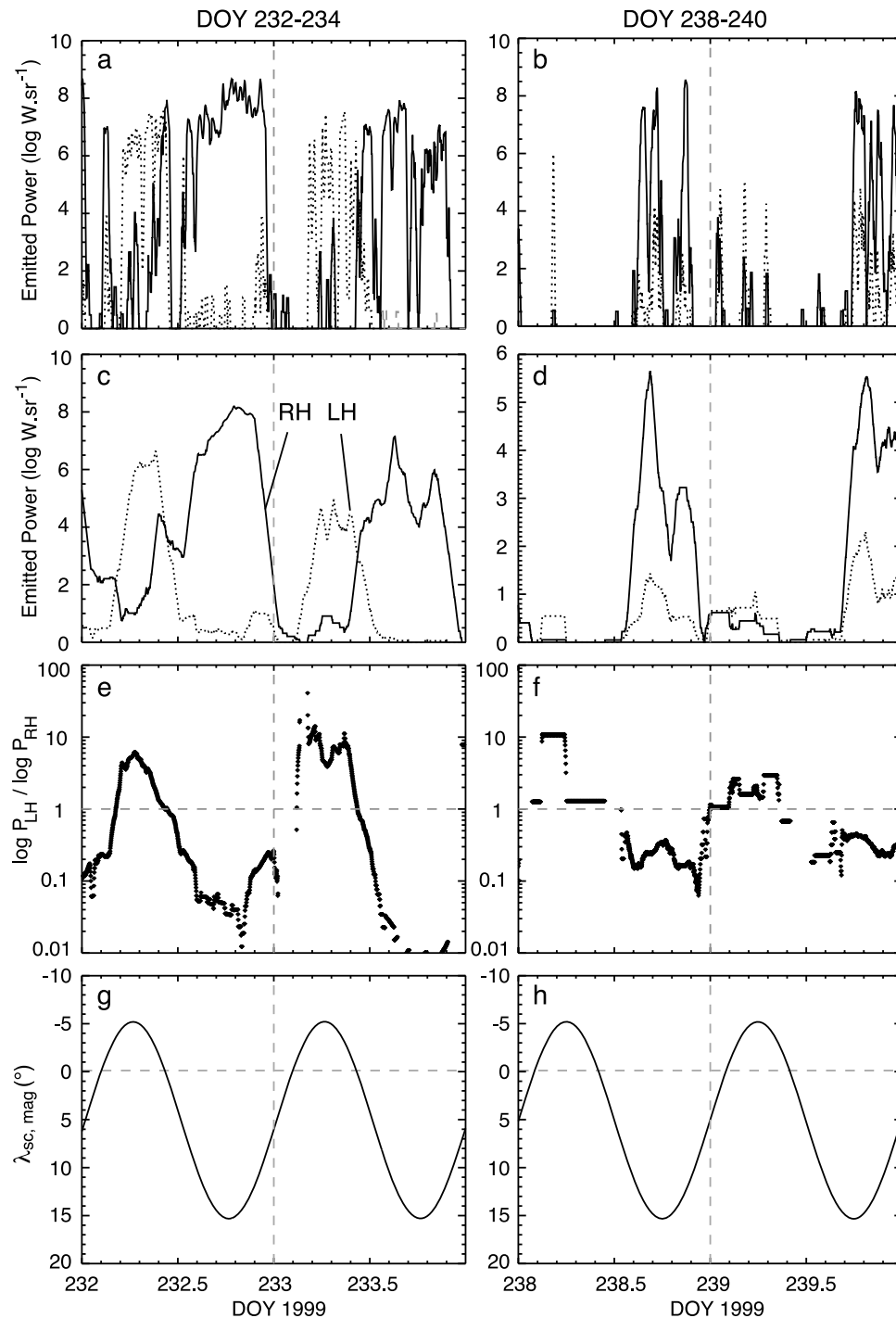


Figure 13. AKR variations at two time scales for (left) DOY 232–234 and (right) DOY 238–240. Time series of RH (solid) and LH (dotted) apparent radiated powers, integrated over the 30–650 kHz range, are smoothed over (a, b) 15 min and (c, d) 3 h. (e, f) Ratio of $\log P_{LH}$ to $\log P_{RH}$, computed from profiles of Figures 13c and 13d. (g, h) Variations of Cassini’s magnetic latitude versus time.

large amplitude (Figure 13e). At the same time, we can see that many emission peaks appearing in the higher temporal resolution plots, 15 min smoothed, occur simultaneously in the RH and LH data (Figure 13a).

[32] During the late period, the RH and LH apparent power variations remain correlated at a 15 min resolution (Figure 13b). They seem to be globally correlated at 3 h resolution (Figure 13d), but the variations of their intensity ratio (Figure 13f) demonstrate that RH and LH power are in fact

anticorrelated with a 24 h period when smoothed over 3 h. This diurnal anticorrelation is not well visible on absolute intensity plots (Figure 13d) because the LH emission is then globally weaker than the RH one. In both early and late periods, the RH to LH power ratio also varies as the magnetic latitude of Cassini $\lambda_{sc,mag}$ (Figures 13g and 13h).

[33] Finally, in Figure 14, we analyze and compare the quality of the organization of RH and LH apparent power variations in a rotating frame and in a frame fixed in LT, respectively. To do so, we compare the RH and LH AKR distributions resulting from the folding of AKR power variations as a function of the subspacecraft magnetic longitude and of the magnetic longitude of the antisolar direction (selected because it is known to have a major role in the terrestrial auroral activity, and hereafter called “submidnight” longitude), respectively. The folding consists of averaging the AKR power measured in the same longitude bins (subspacecraft or submidnight), rotation after rotation. This produces a reconstructed dynamic spectrum, plotted as a function of the selected longitude system in Figure 14. By integrating this dynamic spectrum over the 30–650 kHz range corresponding to the AKR spectral peak, we obtain a reconstructed distribution of the RH and LH integrated apparent power which is plotted as a function of longitude, subspacecraft, or submidnight, respectively. Finally, the integrated power distribution is compared to the magnetic latitude variations (subspacecraft or submidnight). This analysis was performed separately for the brief inbound leg and the long outbound leg (27 rotations) which are located at quite different LT.

[34] The apparent power distributions, once plotted in the longitude system to which the observed emission is bound, are expected to exhibit a narrower and more intense peak than when they are plotted in an unrelated longitude system. In addition, the longitude of the peak must remain the same in the inbound and outbound data set in the correct longitude frame. And finally, the RH (LH) power peak is expected to coincide with the maximum (minimum) magnetic latitude of the spacecraft in the case of a visibility effect. The power cumulated along the brief inbound leg is weak (Figures 14a–14h), with peaks 1 to 2 orders of magnitude lower in LH polarization, and 4 to 6 orders of magnitude lower in the RH one, than over the outbound leg (Figures 14i–14p). The RH inbound distribution cannot even be used. Another difficulty is that the two systems of longitude are not completely random with respect to one another, as Cassini remains almost in a fixed meridian plane (within 1 h LT or so) during each of the period studied, so that the broadening of the peak and its dimming in the wrong longitude system are not expected to be very strong.

[35] Along the outbound leg, the RH power peaks at maximum subspacecraft magnetic latitude (Figures 14i and 14j) and near maximum submidnight magnetic latitude (Figures 14m and 14n). As the two longitude systems differ only by ~ 1.5 h LT along that portion of Cassini’s trajectory, these plots do not allow to decide convincingly which system better organizes the data, but we note that the peak is 20% higher in subspacecraft coordinates. The same is true for LH emission (Figures 14k, 14l, 14o, and 14p). This suggests that visibility effects may dominate the 24 h modulation of AKR. A much stronger evidence is brought by the analysis of the inbound leg. Here, the LH power (Figures 14c, 14d, 14g, and 14h) dominates the RH one (Figures 14a, 14b, 14e, and 14f) by 1 order of magnitude, and is again more consistently organized in subspacecraft coordinates: not only the folded LH power peaks at a higher value in subspacecraft coordinates (compare Figures 14c, 14d, 14g, and 14h), but also this peak occurs at maximum southern magnetic latitude only in subspacecraft coordinates (Figure 14d) and not in submidnight ones (Figures 14h).

[36] We finally note a clear modulation at 12 h in LH data along the outbound leg (Figures 14k and 14l), with two peaks of similar amplitude at each planetary rotation, as also seen in Figure 13d.

5. Discussion

5.1. Average Beaming

[37] Cassini observations of AKR globally confirm the sketch of Figure 2 describing the average AKR beaming from sources approximately fixed in LT, with a few nuances: contrary to the sketch, RH emission is detected before CA. As, for each RPWS/HFR time-frequency measurement, the derived polarization is dominated by that of the strongest point radio source detected at that time and frequency, the RH emission detected before CA cannot be attributed to instrumental cross talk between circular polarizations, but is real RH emission. So it must be concluded that the sketch of Figure 2 describes an average situation but that sporadic emission can be beamed toward the dayside low latitudes.

5.2. Diurnal Modulation: Intrinsic Source Strength Modulation or Visibility Effect?

[38] As already mentioned, one of the main questions arising from this study is the nature of the AKR modulations observed at various time scales, either (A) an intrinsic variation of the source strength (by a variable, LT fixed, or by a rotating triggering effect), or (B) the modulation of a constant source strength by a time-varying visibility factor. In this subsection, we focus on the observed diurnal modulation.

Figure 14. AKR dynamic spectrum and distribution of radiated power integrated over 30–650 kHz resulting from the folding of observed quantities as a function (a–d and i–l) of subspacecraft magnetic longitude and (e–h and m–p) of submidnight magnetic longitude (i.e., magnetic longitude of the antisolar direction). Dynamic spectra (Figures 14a, 14c, 14e, 14g, 14i, 14k, 14m, and 14o) and distributions (Figures 14b, 14d, 14f, 14h, 14j, 14l, 14n, and 14p) are computed separately for RH (Figures 14a, 14b, 14e, 14f, 14i, 14j, 14m, and 14n) and LH (Figures 14c, 14d, 14g, 14h, 14k, 14l, 14o, and 14p) AKR, measured along the inbound (Figures 14a–14h) and outbound (Figures 14i–14p) trajectory. The subspacecraft or submidnight magnetic latitude is superimposed on top of the power distributions (in gray, with scale on the right) in order to compare the relative variations, while subspacecraft magnetic latitude follows the same variation rotation after rotation (Figures 14b, 14d, 14j, and 14l), a broad range of magnetic latitudes is covered by the submidnight point along the outbound leg (Figures 14n and 14p) due to seasonal evolution over the ~ 1 monthlong corresponding interval.

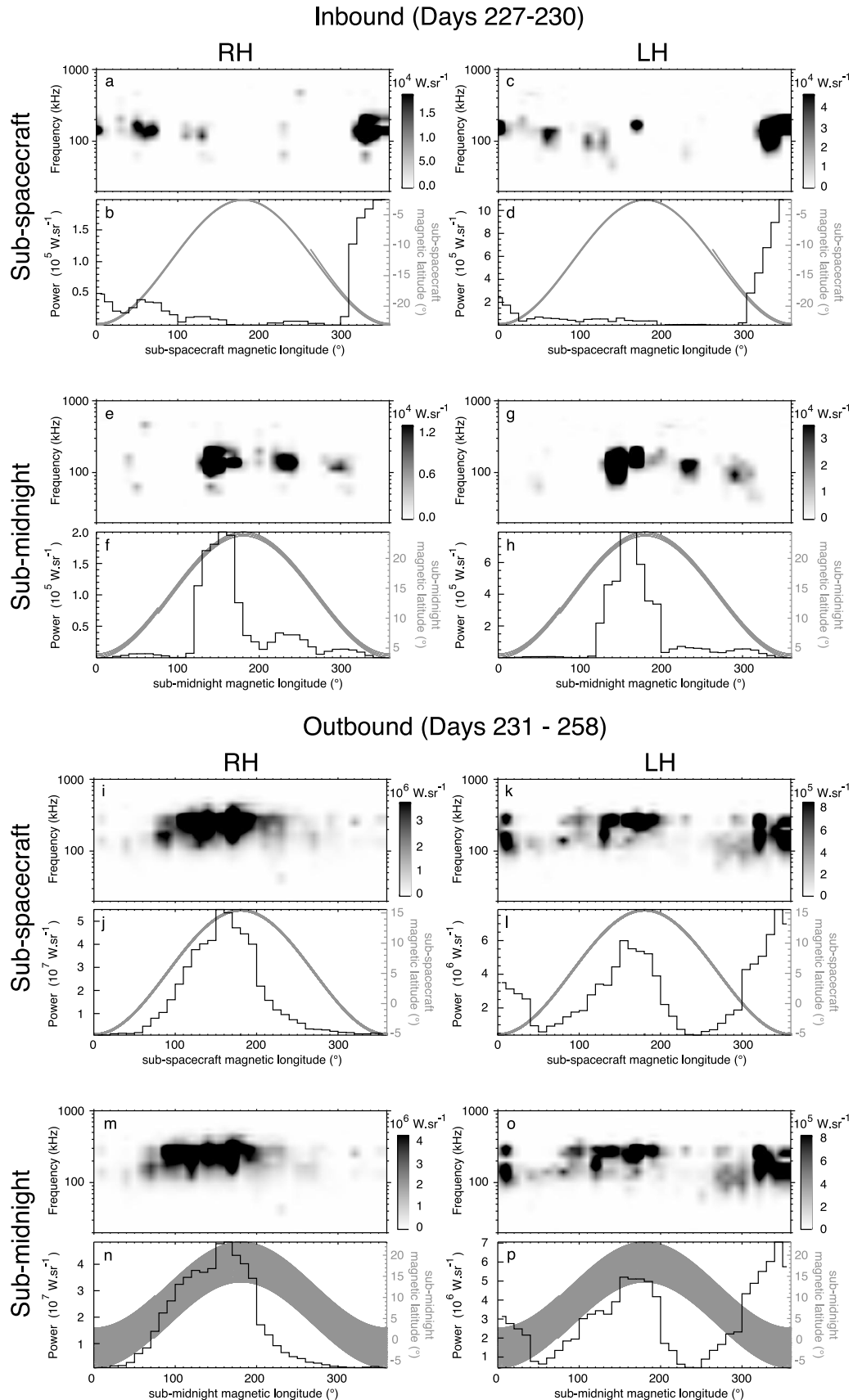


Figure 14

[39] The most significant information here is brought by the identification of the frame of reference which best organizes the data folded at the 24 h periodicity. We have established in section 4 with Figure 14 that the frame that best organizes the data is the one which moves with the spacecraft. This indicates that the cause of the modulation is necessarily a visibility effect, related to a variation of the viewing geometry of the source from the spacecraft.

[40] This disagrees with conclusions of a recent study by *Panchenko et al.* [2009] investigating the AKR diurnal modulation from near-equatorial, pre-midnight observations of the STEREO-B spacecraft, which directly compares to our Cassini data set. *Panchenko et al.* [2009] argue that the diurnal modulation of the observed AKR is an intrinsic modulation of the source strength triggered by diurnal variations of the ionospheric auroral density under solar illumination.

[41] In our case, an essential information is brought by the observations of Cassini from two different LT sectors, before and after the closest approach, and consistent with a single, spacecraft related, reference frame. Consequently, we favor a visibility modulation with 24 h periodicity driven by the precession of the Earth's magnetic axis with respect to the rotational axis, which leads the spacecraft to oscillate around the magnetic equator at the wobbling period.

[42] This visibility modulation is a direct consequence of the nonisotropic AKR beam from each hemisphere, which results from amplification by CMI at large angles from the local magnetic field [*Roux et al.*, 1993; *Ergun et al.*, 1998] followed by refraction at the boundaries of the auroral cavity [*Louarn and Le Quéau*, 1996a; *Pritchett et al.*, 2002] as well as in the near source (≤ 100 km background plasma [*Mutel et al.*, 2008]). This results in an asymmetrical beaming pattern that can statistically fill in a widely open cone centered on the local magnetic field vector. Figure 2 schematically illustrates how the spacecraft periodically comes in and out of the emission cone along its wobbling path in magnetic coordinates. This geometrical interpretation of the visibility modulation (case B₂ above) is further strengthened by the anticorrelation observed between the RH and LH emissions, from the northern and southern polar regions (Figure 5), whose beam alternately reaches the spacecraft, and by the coincidence of the main peaks in the cumulated powers with the maximum (minimum) magnetic latitude of Cassini for the northern RH (southern LH) emissions (Figure 14).

[43] As the wave leaves the auroral region, it may also be refracted/reflected by the plasmasphere if the ray path crosses the dense plasma confined in this region. The effect of the plasmasphere adds to the geometrical visibility and essentially refracts the waves out of the equatorial plane [*Xiao et al.*, 2007]. As the plasmasphere also wobbles at the 24 h period with respect to Cassini, it may also contribute to the diurnal modulation of the recorded AKR power (case B₃ above). In an attempt to estimate the importance of this contribution, we investigated the possible intersections of the line of sight from the radio sources (at various frequencies) to the spacecraft with the plasmasphere during our observations. The plasmasphere has an outermost sharp boundary at a magnetic L shell between ~ 3.5 and ~ 5.5 depending on the magnetic activity index K_p [see *Wolf*, 1995, Figure 10.15]. Using the K_p index archives throughout the observation period, we found that below 150 kHz the line of sight prac-

tically never intersects the plasmasphere after day 232, while at 650 kHz it intersects the plasmasphere most of the time until day 243 and intermittently until day 247. No diurnal modulation of the intersection appears in either case. As, in addition, the observed modulations of AKR power ≤ 150 kHz and ≥ 150 kHz are well correlated, we tend to think that refraction by the plasmasphere plays a minor role in the observed visibility modulation. A more definitive conclusion would require a complete ray-tracing study, out of the scope of this paper.

5.3. Nonperiodic Short-Term Modulation

[44] AKR is found to occur within apparent bursts lasting from 1 to ~ 3 h. They are nonperiodic, but they occur with an average recurrence time of ~ 2 – 4 h (Figures 3, 11, and 13). A previous study suggested their association with substorms [*Kurth et al.*, 2001], which exhibit a similar temporal behavior and which are known to trigger bright auroral emissions. The present study additionally establishes that the nonperiodic northern and southern AKR bursts are correlated at this time scale for larger distances. We can thus infer that visibility effects cannot be involved, and that the observed bursts are due to intrinsic variations of the AKR source strength. As the northern and southern sources are brightening simultaneously despite different local conditions, the intrinsic variations cannot be related to an internal (planetary, atmospheric, ionospheric) process. An external, magnetospheric one, is the only possible trigger, and near midnight, substorms are the most plausible ones.

5.4. Semidiurnal Modulation at 12 h

[45] We also found a 12 h modulation of AKR, which is not detected all the time, but best visible during the late post-encounter interval. At such large distances, the spacecraft travels in regions where visibility conditions are less variable, because the fraction of time that Cassini spent within the "RH & LH" region of Figure 2 is increasingly large. The subsequent 24 h modulation is thus dimmer, so that less prominent modulations may become detectable. This may also explain why this 12 h modulation is mostly seen in LH polarization: as the LH component is indeed detected only from the near-equatorial region, the 24 h modulation due to visibility is much less prominent in LH data. The origin of this fainter modulation is not easy to unambiguously identify. Its detection in power spectra (Figure 11), power profiles (Figure 13), as well as folded dynamic spectra and power distributions (Figure 14) is nonmarginal and cannot be of spurious origin. Then, the source/Cassini geometry is not likely to favor any 12 h filtering effect. We are thus left with the possibility of a semidiurnal physical modulation of the AKR source strength, which is also seen in some of the geomagnetic indices variations (Figure 12). This semidiurnal effect cannot be related to solar wind conditions, nor to the usual substorm activity which varies on time scales of a few hours and which has been considered above to trigger the AKR bursts.

[46] Nevertheless, other auroral processes, such as the geomagnetic activity and substorm occurrence are known to be subject to a similar 12 h modulation. The origin of these modulations are likely to be the same, and related to north-south asymmetries in the magnetosphere induced by the variable obliquity of the Earth's magnetic axis with respect

to the Sun-Earth direction during its rotation. *Russell and McPherron* [1973] suggested that the increased geomagnetic activity could result from increased efficiency of magnetic reconnection at the nose of the magnetopause, which occurs twice a day when the IMF projection on z_{GSM} is extremum (in the Geocentric Solar Magnetospheric system, x points toward the Sun and the xz plane contains the dipole, with z counted positively toward the northern magnetic pole). Alternately, *Kivelson and Hughes* [1990] proposed that the diurnal oscillation of the hinging point of the magnetospheric tail controls the occurrence and magnitude of substorms (which are favored by a large bending of the magnetotail occurring twice per cycle).

[47] A last and different interpretation might come from a possible detection of O mode, neglected in this study. Therefore, the two consecutive LH peaks of Figures 14k and 14l could correspond to southern extraordinary X mode emission and northern ordinary O mode. However, these peaks are only about 8 times lower than the RH peak of Figure 14j, while O mode is generally rather observed to be 1 to 2 orders of magnitude weaker than X mode [*Mellott et al.*, 1984]. We consequently do not favor this explanation, especially considering that a semidiurnal modulation of geomagnetic indices exists.

5.5. From Anticorrelated to Correlated Apparent AKR Emissions

[48] In section 4, we mentioned a puzzling transition from anticorrelated RH and LH observed power variations prior to day 237 ± 1 , to correlated variations after this date (Figures 9 and 10). This transition occurred when Cassini was at $\sim 1500 R_E$ from the Earth, at no particular location along the postencounter trajectory (Figures 1a and 2). Cassini exited the Earth's magnetospheric tail several days earlier, and moved at quasi-constant LT and latitude. No particular change occurred in solar wind conditions around day 237. The only significant but gradual changes occurring along the postencounter trajectory are the increase in distance at $\sim 230 R_E/\text{day}$, and the increasing fraction of time that Cassini spent within the "RH & LH" region of Figure 2 (which may actually have reached 100% beyond a certain point).

[49] The combination of the different types of AKR variability discussed above allows us to explain the observed evolution: the diurnal geometrical modulation of the visibility of northern and southern emissions (section 5.2), as sketched in Figure 2 and evidenced in Figure 9 on the one hand, competes with the intrinsic nonperiodic AKR emission bursts (section 5.3) and the AKR semidiurnal variations observed during the late postencounter phase (section 5.4), on the other hand. We have shown that the diurnal modulation due to the variations of the visibility conditions of the AKR sources dominates in the nearby environment of the Earth. This oscillation, due to the rocking of Earth's magnetic field as seen from Cassini, favored alternate visibility of each hemisphere and thus apparent anticorrelation of detected RH and LH powers (Figure 13, left).

[50] At larger distances during the postencounter interval, where the spacecraft spent an increasing fraction of the time within the "RH & LH" region of Figure 2, we have identified a prominence of the substorm-driven bursts and of the semidiurnal modulations, that we have assigned to the quasi disappearance of the visibility variations which previously

overcame them. The AKR variations which dominate during this period have been attributed to the real source strength variability, either due to substorm occurrences or to a semidiurnal change in the magnetosphere dynamics. As both types of magnetospheric processes affect simultaneously auroral emissions in both hemispheres, AKR RH and LH emissions are consequently observed in phase.

[51] Figure 10 allows us to detail further this interpretation. While the variations of the dominant RH component (due to a trajectory mainly located in the northern magnetic hemisphere) remained correlated to Cassini's magnetic latitude, showing that geometrical visibility in fact modulated the RH emission over the whole encounter, this was not true for the LH emission, for which substorm occurrence and 12 h periodicity became soon the dominant modulations. We also noted that, at the shortest time resolution of our data (90 s), RH and LH fluctuations remained correlated over the entire flyby, even when 3 h averaged powers vary in anticorrelation. This confirms the above interpretations and shows that northern and southern AKR sources are conjugate down to the shortest time scales.

6. Conclusion

[52] The flyby of the Earth by Cassini allowed us to analyze a month of RPWS/HFR homogeneous data on AKR, observed from a quasi-fixed vantage point (Figure 1). Cassini's HFR capability to measure the 4 Stokes parameters of incoming radio waves were used to confirm that AKR is $\sim 100\%$ circularly polarized (Figures 3 and 4), consistent with predominant X mode emission, with RH emission coming from the northern magnetic (southern geographic) hemisphere and LH emission from the southern (northern geographic) one (Figure 2). Polarization properties were used to extract AKR dynamic spectra from RPWS/HFR measurements (Figures 3 and 5), and to build an accurate AKR spectrum (Figure 6) as well as time series of the apparent radiated powers (Figure 9). We have confirmed the illumination patterns of RH and LH AKR sources (Figure 2), and measured the shape of the equatorial edge of the northern and southern beams (Figure 8). Distribution of emitted AKR power was found to be log-normal (Figure 7), in agreement with the nature of the CMI triggering process.

[53] Focussing on AKR temporal modulations, we detected a prominent 24 h modulation, confirmed by STEREO Observations [*Panchenko et al.*, 2009]. Contrary to these authors conclusions, we established that this modulation does not result from an intrinsic variability of the source strength, but that it is primarily due to the varying visibility of northern and southern AKR sources related to the precession of the Earth's magnetic axis (AKR sources being at first order fixed in LT and in magnetic coordinates). We argued that the varying visibility is due to the oscillation of the AKR anisotropic emission beam as seen from Cassini. Varying refraction effects by the oscillating plasmasphere on the AKR source modulation was considered to be a secondary effect. Quantitative evaluation of its amplitude would require a specific ray-tracing study.

[54] We detected a short-term modulation of AKR by substorms, already seen by *Kurth et al.* [2001], but we also showed that sources in both hemispheres are conjugated, probably due to simultaneous particle precipitations in both

hemispheres. The superposition of intrinsic (substorm) and geometrical (visibility) variability leads to a peculiar behavior of RH and LH emissions, switching from an apparent anticorrelation close to Earth to correlation when observed from farther away.

[55] We finally found a 12 h modulation of AKR, usually hidden by the prominent 24 h modulation but detectable for LH emission observed far from Earth, absent in solar wind variations but affecting some geomagnetic indices (especially AU). Although some definitive confirmation is still needed, we suggest that this semidiurnal modulation is real. Among possible origins, we favor variations of magnetic reconnection efficiency or the influence of magnetotail topology, which are indeed expected to be modulated by the Earth rotation and to exhibit diurnal and semidiurnal cycles. Cassini permitted these studies due to its sensitive, well-calibrated HFR receiver, as well as to its slowly changing geometry of observation, very different from that of an orbiting spacecraft in low Earth orbit. The STEREO spacecraft shares the same advantages (vantage points in the ecliptic plane with slowly varying LT) and should enable further measurements, especially the study of the semidiurnal modulation. Further advances in the understanding of AKR beaming and source location will require goniopolarimetric studies and/or visibility simulations, similar to those performed recently for Jupiter [Hess *et al.*, 2008] and Saturn [Lamy *et al.*, 2008b].

[56] **Acknowledgments.** We thank the referees for fruitful exchanges. We acknowledge R. Mutel for his relevant comments, C. Jacquey for discussion on the geomagnetic indices, and A. Zaslavsky for useful explanations on log-normal properties. Solar wind data were obtained from the Omniweb database, and geomagnetic indices were from the International Service of Geomagnetic Indices, through the AMDA (Automated Multi Dataset Analysis) online tool developed by the CDPP (Centre de Données de la Physique des Plasmas). We thank Cassini RPWS engineers at the University of Iowa and the Laboratoire d'Etudes Spatiales et d'Instrumentation en Astrophysique (LESIA) of the Observatory of Paris for support on instrumental questions and ephemeris.

[57] Philippa Browning thanks Emma Bunce and James F. Carbary for their assistance in evaluating this paper.

References

- Alexander, J. K., and M. L. Kaiser (1977), Terrestrial kilometric radiation: 2. Emission from the magnetospheric cusp and dayside magnetosheath, *J. Geophys. Res.*, *82*(1), 98–104, doi:10.1029/JA082i001p00098.
- Benediktov, Y. A., G. G. Getmantsev, and Y. A. Sazonov (1965), Preliminary results of measurements of the intensity of distributed extraterrestrial radio frequency emission at 725 and 1525kc (in Russian), *Kosm. Issled.*, *3*, 614.
- Benson, R. F., and J. Fainberg (1991), Maximum power flux of auroral kilometric radiation, *J. Geophys. Res.*, *96*(A8), 13,749–13,762, doi:10.1029/91JA01172.
- Berthelier, A. (1976), Influence of the polarity of the interplanetary magnetic field on the annual and the diurnal variations of magnetic activity, *J. Geophys. Res.*, *81*(25), 4546–4552, doi:10.1029/JA081i025p04546.
- Borovsky, J. E., R. J. Nemzek, and R. D. Belian (1993), The occurrence rate of magnetospheric-substorm onsets: Random and periodic substorms, *J. Geophys. Res.*, *98*(A3), 3807–3813, doi:10.1029/92JA02556.
- Campbell, W. H. (1996), Geomagnetic storms, the Dst ring-current myth and lognormal distributions, *J. Atmos. Terr. Phys.*, *58*, 1171–1187.
- Cecconi, B. (2009), Comment on “Spectral features of SKR observed by Cassini/RPWS: Frequency bandwidth, flux density and polarization” by Patrick Galopeau *et al.*, *J. Geophys. Res.*, *114*, A07206, doi:10.1029/2007JA012970.
- Cecconi, B., and P. Zarka (2005), Direction finding and antenna calibration through analytical inversion of radio measurements performed using a system of two or three electric dipole antennas on a three-axis stabilized spacecraft, *Radio Sci.*, *40*, RS3003, doi:10.1029/2004RS003070.
- Ergun, R. E., *et al.* (1998), FAST satellite observations of electric field structures in the auroral zone, *Geophys. Res. Lett.*, *25*(12), 2025–2028, doi:10.1029/98GL00635.
- Fischer, G., B. Cecconi, L. Lamy, S.-Y. Ye, U. Taubenschuss, W. Macher, P. Zarka, W. S. Kurth, and D. A. Gurnett (2009), Elliptical polarization of Saturn kilometric radiation observed from high latitudes, *J. Geophys. Res.*, *114*, A08216, doi:10.1029/2009JA014176.
- Gallagher, D. L., and N. Dangelo (1981), Correlations between solar wind parameters and auroral kilometric radiation intensity, *Geophys. Res. Lett.*, *8*(10), 1087–1089, doi:10.1029/GL008i010p01087.
- Gallagher, D. L., and D. A. Gurnett (1979), Auroral kilometric radiation—Time-averaged source location, *J. Geophys. Res.*, *84*(A11), 6501–6509, doi:10.1029/JA084iA11p06501.
- Green, J. L., and D. L. Gallagher (1985), The detailed intensity distribution of the AKR emission cone, *J. Geophys. Res.*, *90*(A10), 9641–9649, doi:10.1029/JA090iA10p09641.
- Green, J. L., S. Boardsen, L. Garcia, S. F. Fung, and B. W. Reinisch (2004), Seasonal and solar cycle dynamics of the auroral kilometric radiation source region, *J. Geophys. Res.*, *109*, A05223, doi:10.1029/2003JA010311.
- Gurnett, D. A. (1974), The earth as a radio source: Terrestrial kilometric radiation, *J. Geophys. Res.*, *79*(28), 4227–4238, doi:10.1029/JA079i028p04227.
- Gurnett, D. A., *et al.* (2004), The Cassini radio and Plasma wave science investigation, *Space Sci. Rev.*, *114*, 395–463.
- Hess, S., B. Cecconi, and P. Zarka (2008), Modeling of Io-Jupiter Decameter Arcs, Emission Beaming and Energy Source, *Geophys. Res. Lett.*, *35*, L13107, doi:10.1029/2008GL033656.
- Huff, R. L., W. Calvert, J. D. Craven, L. A. Frank, and D. A. Gurnett (1988), Mapping of auroral kilometric radiation sources to the aurora, *J. Geophys. Res.*, *93*(A10), 11,445–11,454, doi:10.1029/JA093iA10p11445.
- Kaiser, M. L., J. K. Alexander, A. C. Riddle, J. B. Pearce, and J. W. Warwick (1978), Direct measurements by Voyagers 1 and 2 of the polarization of terrestrial kilometric radiation, *Geophys. Res. Lett.*, *5*(10), 857–860, doi:10.1029/GL005i010p00857.
- Kasaba, Y., H. Matsumoto, K. Hashimoto, and R. R. Anderson (1997), The Angular distribution of auroral kilometric radiation observed by the GEOTAIL spacecraft, *Geophys. Res. Lett.*, *24*(20), 2483–2486, doi:10.1029/97GL02599.
- Kivelson, M. G., and W. J. Hughes (1990), On the threshold for triggering substorms, *Planet. Space Sci.*, *38*, 211–220.
- Kumamoto, A., T. Ono, M. Iizima, and H. Oya (2003), Seasonal and solar cycle variations of the vertical distribution of the occurrence probability of auroral kilometric radiation sources and of upflowing ion events, *J. Geophys. Res.*, *108*(A1), 1032, doi:10.1029/2002JA009522.
- Kurth, W. S., G. B. Hospodarsky, D. A. Gurnett, M. L. Kaiser, J. Wahlund, A. Roux, P. Canu, P. Zarka, and Y. Tokarev (2001), An overview of observations by the Cassini radio and plasma wave investigation at Earth, *J. Geophys. Res.*, *106*(A12), 30,239–30,252, doi:10.1029/2001JA900033.
- LaBelle, J., R. A. Treumann, M. H. Boehm, and K. Gewecke (1989), Natural and man-made emissions at 1.0–5.6 MHz measured between 10 and 18 Re, *Radio Sci.*, *24*(6), 725–737, doi:10.1029/RS024i006p00725.
- Lamy, L., R. Prangé, B. Cecconi, and P. Zarka (2007), Diurnal modulation of AKR observed by Cassini/RPWS and consequences on magnetospheric dynamics, paper presented at Magnetospheres of the Outer Planets, Southwest Res. Inst., San Antonio, Tex.
- Lamy, L., P. Zarka, B. Cecconi, R. Prangé, W. S. Kurth, and D. A. Gurnett (2008a), Saturn kilometric radiation: Average and statistical properties, *J. Geophys. Res.*, *113*, A07201, doi:10.1029/2007JA012900.
- Lamy, L., P. Zarka, B. Cecconi, S. Hess, and R. Prangé (2008b), Modeling of Saturn kilometric radiation arcs and equatorial shadow zone, *J. Geophys. Res.*, *113*, A10213, doi:10.1029/2008JA013464.
- Louarn, P., and D. Le Quéau (1996a), Generation of the auroral kilometric radiation in plasma cavities: II. The cyclotron maser instability in small size sources, *Planet. Space Sci.*, *44*, 211–224.
- Louarn, P., and D. Le Quéau (1996b), Generation of the auroral kilometric radiation in plasma cavities: I. Experimental study, *Planet. Space Sci.*, *44*, 199–210.
- Mellott, M. M., W. Calvert, R. L. Huff, D. A. Gurnett, and S. D. Shawhan (1984), DE-1 observations of ordinary mode and extraordinary mode auroral kilometric radiation, *Geophys. Res. Lett.*, *11*(12), 1188–1191, doi:10.1029/GL011i012p01188.
- Mutel, R. L., I. W. Christopher, and J. S. Pickett (2008), Cluster multi-spacecraft determination of AKR angular beaming, *Geophys. Res. Lett.*, *35*, L07104, doi:10.1029/2008GL033377.
- Panchenko, M., J. Hanasz, and H. O. Rucker (2008), Estimation of linear wave polarization of the auroral kilometric radiation, *Radio Sci.*, *43*, RS1006, doi:10.1029/2006RS003606.

- Panchenko, M., et al. (2009), Daily variations of auroral kilometric radiation observed by STEREO, *Geophys. Res. Lett.*, *36*, L06102, doi:10.1029/2008GL037042.
- Pritchett, P. L., R. J. Strangeway, R. E. Ergun, and C. W. Carlson (2002), Generation and propagation of cyclotron maser emissions in the finite auroral kilometric radiation source cavity, *J. Geophys. Res.*, *107*(A12), 1437, doi:10.1029/2002JA009403.
- Roux, A., et al. (1993), Auroral kilometric radiation sources: In situ and remote observations from Viking, *J. Geophys. Res.*, *98*(A7), 11,657–11,670, doi:10.1029/92JA02309.
- Russell, C. T., and R. L. McPherron (1973), The magnetotail and substorms, *Space Sci. Rev.*, *15*, 205–266.
- Samara, M., J. LaBelle, and I. H. Cairns (2008), Statistics of auroral Langmuir waves, *Ann. Geophys.*, *26*, 3885–3895.
- Shefov, N. N., A. I. Semenov, and O. T. Yurchenko (2006), Empirical model of variations in the OI 630 nm emission: 1. Intensity, *Geomagn. Aeron.*, *46*, 236–246.
- Treumann, R. A. (2000), Planetary radio emission mechanisms: A tutorial, in *Radio Astronomy at Long Wavelengths*, *Geophys. Monogr. Ser.*, vol. 119, edited by R. G. Stone et al., pp. 13–26, AGU, Washington, D. C.
- Wolf, R. A. (1995), Magnetospheric configuration, in *Introduction to Space Physics*, edited by M. G. Kivelson and C. T. Russell, chap. 10, pp. 288–329, Cambridge Univ. Press, Cambridge, U. K.
- Wu, C. S. (1985), Kinetic cyclotron and synchrotron Maser instabilities: Radio emission processes by direct amplification of radiation, *Space Sci. Rev.*, *41*, 215–298.
- Wu, C. S., and L. C. Lee (1979), A theory of the terrestrial kilometric radiation, *Astrophys. J.*, *230*, 621–626.
- Xiao, F., L. Chen, H. Zheng, and S. Wang (2007), A parametric ray tracing study of superluminous auroral kilometric radiation wave modes, *J. Geophys. Res.*, *112*, A10214, doi:10.1029/2006JA012178.
- Zarka, P. (1998), Auroral radio emissions at the outer planets: Observations and theories, *J. Geophys. Res.*, *103*(E9), 20,159–20,194, doi:10.1029/98JE01323.
- Zarka, P., B. Cecconi, and W. S. Kurth (2004), Jupiter's low-frequency radio spectrum from Cassini/Radio and Plasma Wave Science (RPWS) absolute flux density measurements, *J. Geophys. Res.*, *109*, A09S15, doi:10.1029/2003JA010260.

B. Cecconi, R. Prangé, and P. Zarka, LESIA, Observatoire de Paris, CNRS, UPMC, Université Paris Diderot, 5 Place Jules Janssen, F-92190 Meudon, France.

L. Lamy, Space and Atmospheric Physics, Imperial College London, Prince Consort Road, London SW72AZ, UK.